Chinese Physics Letters

LETTER

Acoustic Reconfigurable Metagratings with High Quality Factor for Anomalous Wavefront Control

Cite as: Fu Xu *et al*. 2026 *Chin. Phys. Lett.* **43** 061002

DOI CSTR

Recommended Articles

Bound States in the Continuum of Infinite Quality Factor in Finite Unit Cells
Hua-Wei Liang, Yuan-Zhi Liu, Yu-Jia Zeng, Yang-Jian Cai, and Ting-Yin Ning
Chin. Phys. Lett. **42**, 080401 (2025)

Anomalous Acoustic Plasmons in Two-Dimensional Over-Tilted Dirac Bands
Chang-Xu Yan, Furu Zhang, Chao-Yang Tan, Hao-Ran Chang, Jianhui Zhou, and Yugui Yao
Chin. Phys. Lett. **43**, 040707 (2026)

Intelligent Reconfigurable Skyrmion-Based Multi-Port Logic Device for In-Memory Computing
Fuhao Zou, Ziyuan Liu, Zijing Zhao, Muhammad Humayun, Chundong Wang, and Xiaolei Wang
Chin. Phys. Lett. **43**, 030802 (2026)

AI-Driven Acoustic Metamaterials for Pixel-Accurate Sound Insulation Control
Kaijing Liu, Yihuan Zhu, Jiachen Meng, Ruizhi Dong, Xu Wang, and Yong Li
Chin. Phys. Lett. **43**, 021001 (2026)

Two-Stage Training Method for High-Quality Reconstruction in Single-Pixel Imaging
Hui Shao, He Huang, Yu-Xiao Wei, Hui-Juan Zhang, Zhao-Hua Yang, and Yuan-Jin Yu
Chin. Phys. Lett. **41**, 124202 (2024)

Selective Area Growth of High-Quality In-Plane GaAs Nanowires and Nanowire Networks by Molecular Beam Epitaxy on Ge Substrates
Fengyue He, Xiyu Hou, Xiuming Dou, Yukun Yin, Dong Pan, and Jianhua Zhao
Chin. Phys. Lett. **42**, 067502 (2025)

iopscience.iop.org/cpl | cpl.iphy.ac.cn

A series journal of Chinese Physical Society distributed by IOP Publishing

Chinese Physics Letters

Chin. Phys. Lett. **43** 061002 (2026)

LETTER

DOI: 10.1088/0256-307X/43/6/061002
CSTR: 32039.14.0256-307X.43.6.061002

Acoustic Reconfigurable Metagratings with High Quality Factor for Anomalous Wavefront Control

Fu Xu(徐傅)[1,†], MengRu Jiang(江梦茹)[1,†], Yu Chen(陈雨)[1], Junyi Yang(杨俊义)[1], Zhanlei Hao(郝占磊)[2,*], and Yadong Xu(徐亚东)[1,*]

[1]School of Physical Science and Technology & Jiangsu Key Laboratory of Frontier Material Physics and Devices, Soochow University, Suzhou 215006, China
[2]School of Electronic & Information Engineering, Nanjing University of Information Science & Technology, Nanjing 210044, China

[†]These authors contributed equally to this work.
[*]Corresponding authors. Email: zhanleihao@nuist.edu.cn; ydxu@suda.edu.cn

Acoustic resonance metasurfaces have emerged as versatile platforms for the precise manipulation of acoustic waves, yet existing designs suffer from fundamental trade-offs among reconfigurability, structural complexity, and resonance quality factors (*Q*). Here, we theoretically propose and experimentally demonstrate a structural design of acoustic reconfigurable metagratings (ARMs) that achieves a high-*Q* Fano resonance via transverse translation of a tunable baffle. This mechanism is enabled by dynamic coupling between discrete local dark modes (first-order guided modes) and continuous bright modes (fundamental guided modes) confined within grooves, creating a pronounced Fano resonance. In contrast to traditional static metagratings, this device enables reversible switching between the state of perfect specular reflection and anomalous reflection using only a subwavelength displacement of the tunable baffle. Furthermore, we analytically elucidate the mechanism of Fano resonance in ARMs and derive the expression for the resonance condition. All theoretical predictions are rigorously validated through full-wave simulations and experimental measurements. This work establishes a paradigm for designing high-*Q* acoustic components with tunable functionality, opening new avenues for applications in ultrasonic sensing and information processing.

Introduction

Effective manipulation of wave phenomena, including refraction, reflection, and propagation, remains a hot research topic in optics and acoustics [1–7]. Notably, anomalous reflection, a critical capability for high-efficiency lidar [8,9], spectrometers [10,11], metalenses [12,13], and electromagnetic cloaks [14], has garnered significant attention. While metasurfaces [15–23], engineered metamaterials with subwavelength structures, offer unprecedented control over wavefronts via tailored resonances, their practical utility is often hindered by surface impedance mismatch, leading to suboptimal conversion efficiency. To address this challenge, metagratings [24–28], arrays of discrete scatterers, have been developed to suppress higher-order diffraction, thereby enhancing the efficiency of desired diffraction orders while maintaining compact form factors. However, existing metagrating designs struggle to achieve both high efficiency and dynamic configurability, particularly in acoustics [29–33].

Existing resonant metagratings suffer from either intricate or fixed architectures or insufficient resonance quality factors (Q) [34,35]. The former imposes prohibitive fabrication costs and restricts scalability, while the latter results in broadened resonance linewidths and diminished wave–matter interactions—constraints that severely limit practical deployment. To address these limitations, there is an urgent need for high-Q metagratings featuring simplified, yet functionally robust, architectures to improve both wave-manipulation efficiency and operational stability. Their exceptional frequency selectivity renders them ideal for high-precision spectroscopy, large-capacity optical communications, and multifunctional sensing/imaging systems. Moreover, programmable reconfiguration of metagratings via parameter modulation, such as geometric tuning, offers transformative potential for on-demand information-processing devices. For instance, recent studies have demonstrated that adjusting the length of a single air groove in a reflective phase-gradient metagrating can trigger localized Fabry–Pérot (FP) resonance, enabling dynamic switching between anomalous and specular reflections at target frequencies [36]. Early metagrating designs primarily relied on fundamental guided modes within subwavelength unit cells (i.e., grooves) [37–39]. Recent studies, however, have revealed that higher-order guided modes also play a critical role in metagrating functionality [40]. Among these, Fano resonance arising from interference between discrete and continuum states within structural elements offers a new mechanism for achieving anomalous reflection. This approach enables wavefront manipulation without phase gradients, significantly simplifying metasurface design. Owing to its strict excitation conditions, precise geometric requirements, and environmental sensitivity, Fano resonance with high-Q characteristics [41] provides a perfect solution for multifunctional wavefront manipulation.

In this work, we theoretically propose and experimentally demonstrate a planar reflective acoustic reconfigurable metagrating (ARM) composed of periodic air grooves and a laterally movable baffle (Fig. 1). Through simple, subwavelength mechanical adjustment, i.e., transverse translation of the baffle, we achieve Fano resonance with a high Q, enabling dynamic wavefront control with near 100% conversion efficiency. Numerical simulations and analytical calculations reveal that precise subwavelength positioning of the baffle selectively activates the Fano resonance, thereby reconfiguring the ARM's functionality from specular to anomalous reflection. By fitting the simulated reflection-phase spectra at 30° incidence, we extract a quality factor $Q = 293$, directly corroborating the pivotal roles of discrete–continuum modal interference and Fano lineshape formation. Experimentally, we demonstrate dynamic beam steering and pronounced frequency selectivity at 3430 Hz, aligning with theoretical predictions.

Results and Discussions

Figure 1 shows the structural schematic of the proposed ARMs, and the operating frequency is $f_0 = 3430$ Hz. At this operating frequency, certain resin materials can be treated as acoustically rigid. The structure comprises alternating rigid segments (gray regions) and air grooves (white regions), with a grating period p equaling the

Received 13 April 2026; accepted 11 May 2026; published 22 June 2026
© 2026 Chinese Physical Society and IOP Publishing Ltd. All rights, including for text and data mining, AI training, and similar technologies, are reserved.

Check for updates

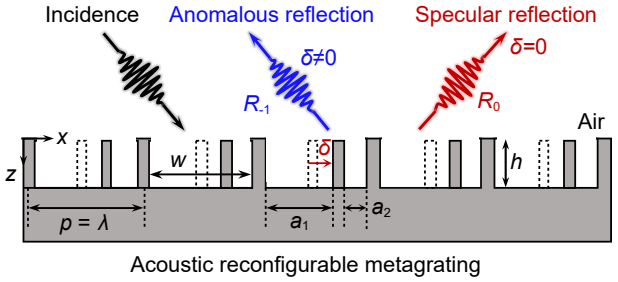

Fig. 1. Structural schematic of ARMs. A periodic subwavelength grating, whose period p equals the incident wavelength λ. Within each unit cell, an air groove of depth h is split by a movable baffle into two sections of widths a_1 and a_2. Black, blue, and red arrows denote the incident, anomalous reflected ($n=-1$), and specularly reflected ($n=0$) waves, respectively. Translating the baffle rightward breaks symmetry, forming a resonant metagrating and enabling anomalous reflection.

operational wavelength $\lambda = p = 10$ cm. Each unit cell features an air groove with width w and duty cycle $w/p = 0.9$. A movable baffle (gray frame) partitions the groove into two sections with widths a_1 and a_2. The groove depth is $h = 0.9p$. When the movable baffle is centered (i.e., $a_1 = a_2 = 0.4p$), the system preserves spatial inversion symmetry. Considering a sound beam incident at an angle of 30° with wavelength λ and free-space wave number $k_0 = 2\pi/\lambda$, the incident wave undergoes nearly perfect specular reflection upon interacting with the structure. Notice that the design of this metagrating is based on two media with a significant impedance mismatch: waves can propagate freely in one medium, while the other provides a hard boundary condition. In fact, beyond sound waves, this structure also exhibits excellent capabilities in manipulating other forms of waves. For instance, if fabricated using metallic materials, it can effectively control electromagnetic waves as well. Since the harnessed material is rigid, each subwavelength air groove can be considered as a waveguide. For ARMs composed of discrete subwavelength grooves, the wave manipulation can be predicted by a formula involving superlattices [42,43],

$$k_x^{\text{in}} = k_x^{\text{out}} - nG, \tag{1}$$

where k_x^{in} and k_x^{out} denote the tangential wavevector components of the incident and scattered waves, respectively, n is the diffraction order, and $G = 2\pi/p$ is the reciprocal lattice vector. When the baffle is centered, the two symmetric grooves in each unit cell reduce the effective period to $0.5p$, which equals half the wavelength, thereby suppressing all higher-order diffraction and allowing only the $n=0$ order to propagate [44,45].

Typically, lateral translation of the baffle by a subwavelength distance δ ($\delta < 0.2p$)—either to the right or left—breaks the spatial inversion symmetry between the dual grooves, restoring the effective grating period to p and selectively activating the $n=-1$ diffraction order. This spatial inversion asymmetry widens the left groove's width, allowing more guided modes within the groove. When δ is tuned within a critical range, a sharp Fano resonance emerges, peaking at $\delta = 0.116p$, arising from interference between a discrete dark mode and the continuum of radiative bright modes. This resonance generates a standing wave in the expanded waveguide, redistributing energy from the suppressed specular reflection into the $n=-1$ diffraction order with near-unity efficiency, thereby enabling perfect anomalous reflection. Numerical simulations using COMSOL Multiphysics quantitatively validate this phenomenon. As shown in Fig. 2(a), by systematically varying the baffle translation distance δ across incident angles θ_{in}, we observe R_0 dropping to 0 at $\theta_{\text{in}} = 30°$ and $\delta = 0.116p$, while maintaining $R_0 > 95\%$ in non-resonant configurations. A contour plot of θ_{in} versus $R_0 = 20\%$ baseline [Fig. 2(a)] reveals that θ_{in} spans 30°–56.5°, with R_0 effectively suppressed by strategic δ tuning. Concurrently, figure 2(b) plots R_{-1}, showing synchronized enhancement: R_{-1} surpasses 99.9% at the R_0 dip, confirming reciprocal mode switching. To elucidate this transition, figures 2(c) and 2(d) presents simulated scattered fields at $\theta_{\text{in}} = 30°$ for $\delta = 0$ and $\delta = 0.116p$, respectively. At $\delta = 0$, specular reflection dominates ($R_0 > 99.9\%$); at $\delta = 0.116p$, anomalous reflection peaks ($R_{-1} > 99.9\%$), accompanied by marked local field enhancement [red dashed box in Fig. 2(d)], which validates resonance activation.

The above field analysis indicates that in the symmetry-broken structure, the Fano resonance in the waveguide has the remarkable feature of local field enhancement. In such systems, interference between a discrete dark mode and a continuum bright mode background generates asymmetric Fano profiles, whose resonance curves adhere to the following relation [46],

$$R(\omega) = D^2 \frac{(q+\Omega)^2}{(1+q^2)} + B, \tag{2}$$

where D is an amplitude scaling factor, q is the asymmetry parameter, and B accounts for the background contribution. $\Omega = 2(\omega - \omega_0)/\Gamma$, where ω_0 is the resonance frequency and Γ is the resonance width. The Q-factor of the Fano resonance satisfies $Q = \omega_0/\Gamma$. As depicted in Fig. 3(a), displacing the movable baffle disrupts spatial inversion symmetry, inducing distinct propagating modes in the dual waveguides: the left wide groove supports both the symmetric fundamental guided mode (bright mode) and the anti-symmetric first-order guided mode (dark mode), while the right narrow groove exclusively sustains the fundamental mode, suppressing higher-order evanescent modes. We calculated the dispersion relation of the left wide groove at $f = f_0$, as shown in Fig. 3(b). The gray background demarcates the study scope. For $\delta < 0.1p$, the fundamental mode wavenumber β_0 remains real, whereas β_1 (first-order guided mode) resides in the imaginary domain—indicating purely evanescent behavior. Beyond $\delta > 0.1p$, β_1 transitions to real values, signifying the onset of propagating first-order modes. Our analysis reveals that dark–bright mode interference triggers Fano resonance when β_1 satisfies

$$2h\beta_1 = (2N-1)\pi. \tag{3}$$

Accordingly, $\beta_m = \text{Sqrt}[k_0^2 - m\pi/(\delta + 0.4p)]$ and N is a positive integer defining the standing-wave antinode count in the wide waveguide [Fig. 2(d)]. Setting $N=1$, we calculate that $\delta = 0.120p$, which is close to the simulated value. This condition reflects half-wavelength resonance in the wide groove, analogous to FP-cavity-mediated mode coupling. Therefore, under the condition of a fixed structure, we can observe a very strong Fano resonance on the frequency spectrum, even though the metagrating structure was designed at 3430 Hz.

On the other hand, coupled-mode theory is developed to calculate the reflection coefficients of different diffraction orders of ARMs, to further explore the influence of propagation modes in ARMs on their diffraction behavior. In the air region ($z > 0$), the pressure field is composed of the sum of the incident wave and the scattered wave. According to the classical Rayleigh expansion, the total pressure field can be expressed as [47,48]

$$P_1 = \sum_n \left[\delta_{n,0} \exp(\text{i}k_z^n z) + r_n \exp(-\text{i}k_z^n z)\right] \exp(\text{i}\alpha_n x), \tag{4}$$

where $\delta_{n,0}$ is the Kronecker delta, $\alpha_n = k_0 \sin\theta_{\text{in}} + nG$ and $k_z^n = \text{Sqrt}(k_0^2 - \alpha_n^2)$ denote the x and z components of the wavevector of the nth diffraction order, respectively. r_n is the reflection coefficient of the nth order, k_0 is the free-space wavenumber, and θ_{in} is the incidence angle. For the investigated metagrating, where p is comparable to λ, only the -1st, 0th, and $+1$st diffraction orders need to be considered. The normal velocity field is derived from $-\text{i}\omega\rho v_z = \partial P/\partial z$,

$$v_{z,1} = \frac{-1}{w\rho_0} \sum_n k_z^n \left[\delta_{n,0} \exp(\text{i}k_z^n z) - r_n \exp(-\text{i}k_z^n z)\right] \exp(\text{i}\alpha_n x), \tag{5}$$

where ρ_0 is the free-space mass density. Similarly, in the metagrating region, the pressure and velocity fields in the jth air groove can be obtained by following equations:

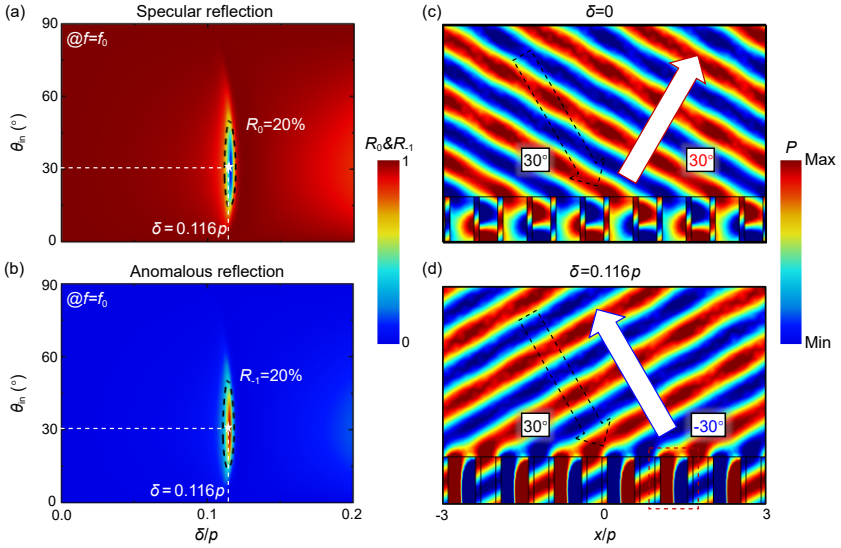

Fig. 2. Numerical simulation results. (a) and (b) The specular reflection efficiency (R_0) and anomalous reflection efficiency (R_{-1}) of ARMs as functions of θ_{in} and δ, respectively. The black dashed lines in (a) and (b) represent the contours of $R_0 = 20\%$ and $R_{-1} = 80\%$, respectively. The valleys of R_0 and peaks of R_{-1} coincide at $\theta_{in} = 30^\circ$ and $\delta = 0.116p$. (c) and (d) The scattered pressure fields of ARMs under normal plane wave incidence when $\delta = 0$ and $\delta = 0.116p$, respectively. The black dashed arrow indicates the incident wave direction (30°), the red arrow denotes the specular reflection direction (30°), and the blue arrow represents the anomalous reflection direction (−30°).

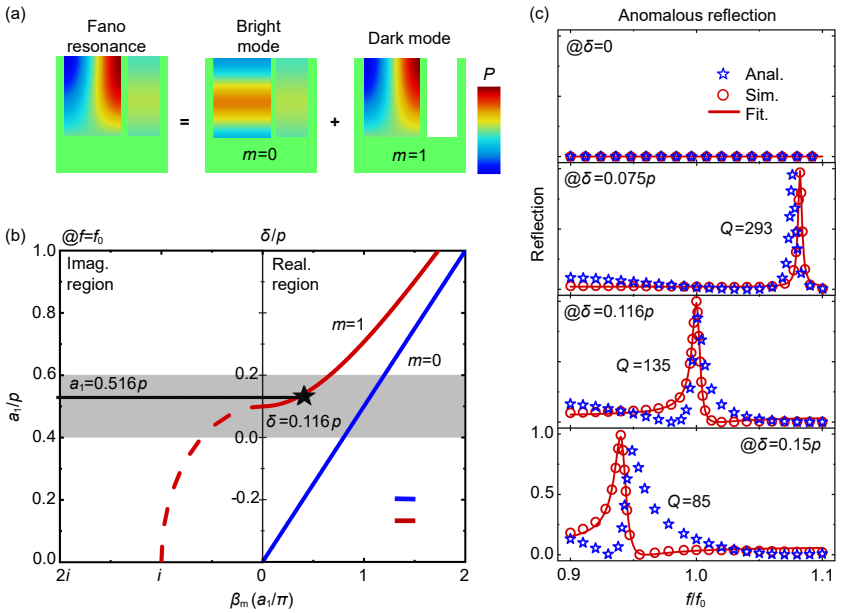

Fig. 3. (a) Schematic of guided modes in the unit cell, including the fundamental propagating mode and the first-order guided mode. (b) The dispersion relation between β_m in the wide waveguide and a_1, where the right (left) panel shows the real (imaginary) part of β_m at $f = f_0$, and the gray area indicates the study scope. (c) Response of ARMs with different δ to incident waves of varying frequencies at $\theta_{in} = 30^\circ$, where both the scatter points and the curve represent R_{-1}.

$$P_{2,j} = \sum_m A_{m,j}\cos[\beta_{m,j}(z-h)]\cos\left[\frac{m\pi}{w_j}(x-R_j)\right], \tag{6}$$

$$v_{z,2,j} = \sum_m \frac{-\mathrm{i}}{w\rho_0}A_{m,j}\beta_{m,j}\sin[\beta_{m,j}(z-h)]\cos\left[\frac{m\pi}{w_j}(x-R_j)\right], \tag{7}$$

where m and j denote the guided mode order and the index of the air groove, respectively, indicating that the propagating modes may differ among distinct grooves. $A_{m,j}$ and $\beta_{m,j}$ are the amplitude coefficient and propagation constant, respectively, of the mth order mode in the jth air groove, satisfying $\beta_{m,j} = \mathrm{Sqrt}[k_0^2 - (m\pi/a_j)^2]$. a_j is the cross-sectional width of the jth air groove, and R_j denotes the coordinate of its left boundary. By enforcing continuity of the acoustic pressure and particle velocity at the interface between the air region and the metagrating ($z = 0$) and applying modal orthogonality through integration, a set of analytical equations can be derived,

$$\sum_n \frac{\delta_{n,0}+r_n}{C_1}D_1 = \frac{A_{m,1}w_1}{2}(\delta_{m,0}+1)\cos(\beta_{m,1}h), \tag{8}$$

$$\sum_n \frac{\delta_{n,0}+r_n}{C_2}D_2 = \frac{A_{m,2}w_2}{2}(\delta_{m,0}+1)\cos(\beta_{m,2}h), \tag{9}$$

$$\sum_j\sum_m \frac{A_{m,j}\beta_{m,j}\sin(\beta_{m,j}h)}{(m\pi/w_j)^2-\alpha_n^2}D_\lambda^* = \mathrm{i}pk_z^n(\delta_{n,0}-r_n), \tag{10}$$

where $C_\gamma = [(m\pi/a_\gamma)^2 - \alpha_n^2]/(\mathrm{i}\alpha_n)$ and $D_\gamma = \cos(m\pi)\exp(\mathrm{i}\alpha_n d_{2\gamma}) - \exp(\mathrm{i}\alpha_n d_{2\gamma-1})$. Here, d_1 and d_3 are x-coordinates of the left boundaries of the two air grooves, while d_2 and d_4 correspond to their right boundaries, respectively. By numerically solving the system of

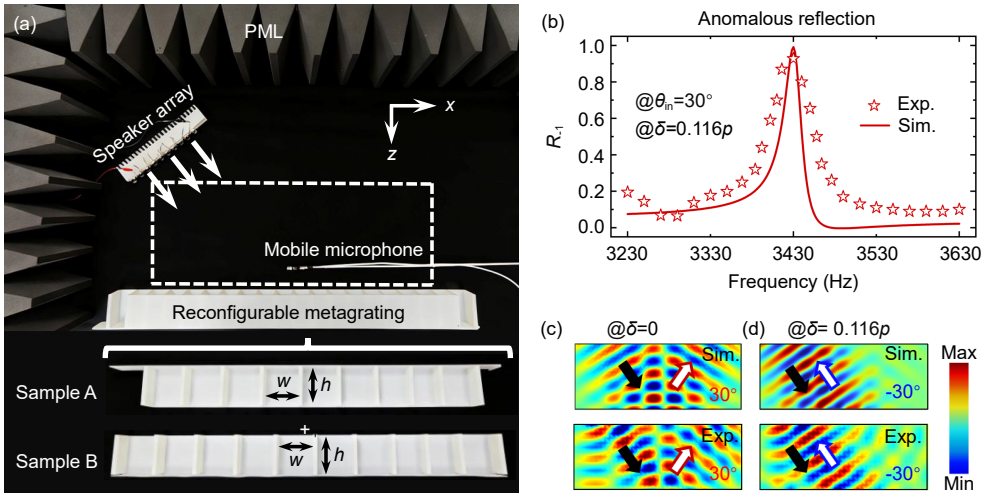

Fig. 4. Acoustic experiment on anomalous wavefront control based on ARMs. (a) Schematic of the experimental setup. (b) The relationship between R_{-1} and frequency at $\theta_{in} = 30^\circ$ and $\delta = 0.116p$. The simulated and measured acoustic pressure fields at $\theta_{in} = 30^\circ$ for (c) $\delta = 0$ and (d) $\delta = 0.116p$.

equations, the reflection coefficients for each diffraction order can be obtained.

We show the reflection spectra of $n = -1$ (anomalous reflection) under different δ tunings in Fig. 3(c), where the red circles are the simulation results, the red curves represent fits to the asymmetric Fano line shape based on Eq. (2), and the blue stars show the analytically calculated results. The excellent agreement among simulation, Fano fitting, and theoretical analysis confirms the characteristic interference origin of the resonance and validates the discrete–continuum coupling model. Specifically, at $\delta = 0$, ARMs exhibit pronounced symmetry, suppressing Fano resonance excitation. Adjusting δ to $0.075p$ induces a resonance peak at $\omega_0 = 1.08 f_0$ with $Q = 293$, and the fitting yields $q \to +\infty$, $D = 0$, $B = 0.021$, and $\Gamma = 0.0037 f_0$; further tuning to $\delta = 0.116p$ shifts the peak to $\omega_0 = f_0$ ($Q = 135$), and yields $q = -2.27$, $D = 0.43$, $B = 0$, and $\Gamma = 0.0074 f_0$; finally, at $\delta = 0.15p$, the fitting yields $q = 1.77$, $D = 0.54$, $B = 0$, $\omega_0 = 0.94 f_0$ with $Q = 85$, and $\Gamma = 0.011 f_0$. It is clear that as δ increases, the resonant frequency decreases and the Q-factor declines. Moreover, all resonances satisfy the predicted resonance peak position of Eq. (3), confirming the excitation conditions of Fano resonance. Notably, the numerical simulations align perfectly with analytical calculations, and the background scattering amplitudes (B) are all less than 0.01, validating the dominant role of fundamental propagating and first-order guided mode coupling in diffraction control.

Acoustic experiments are conducted in a 2D waveguide to validate anomalous wavefront control based on ARMs. The ARMs sample was fabricated using 3D printing technology, and the experimental setup is shown in Fig. 4(a). The sample consists of 10 unit cells, each comprising an air groove and a movable baffle. The inset illustrates that the sample is assembled from two identical halves, ensuring that all baffles across the entire structure can be translated simultaneously and uniformly by simply adjusting a single sliding plate. The sample is made of a commercial photosensitive resin with a flexural modulus of 2700 MPa, a tensile modulus of 2600 MPa, and a density of approximately 1.1 g/cm^3. Owing to the significant acoustic impedance mismatch between the solid material and the surrounding air, the sample can be treated as a rigid acoustic boundary. A sound beam of 25 cm width was generated by a speaker array and incident on the sample at $\theta_{in} = 30^\circ$. The acoustic pressure field within the white rectangular region indicated in Fig. 4(a) was mapped using a mobile microphone scanned with a step size of 0.2 cm. The entire setup was mounted on an optical table, sandwiched between two transparent acrylic plates, and surrounded by acoustic absorbing foam. This foam acts as an effective perfectly matched layer, significantly suppressing unwanted environmental reflections and minimizing their interference with the measurements. Under these experimental conditions, the baffle displacement was first set to $\delta = 0.116p$, and R_{-1} was measured as a function of incident frequency, as shown in Fig. 4(b). Stars and curves represent experimental and simulated results, respectively. It is evident that the anomalous reflection efficiency increases to over 90% at the resonance frequency ($f_0 = 3430$ Hz), while it drops significantly away from resonance. With the operating frequency fixed at $f = 3430$ Hz, we measured the acoustic pressure field for $\delta = 0$ and $\delta = 0.116p$, respectively, as shown in Figs. 4(c) and 4(d). Both simulations and experimental results clearly demonstrate that when $\delta = 0$, ARMs exhibit conventional specular reflection, with an experimentally measured reflection efficiency of 80%. In contrast, when $\delta = 0.116p$, the reflection behavior switches to anomalous reflection, achieving a measured efficiency of 91%. Thus, the experimental results validate that a simple translational adjustment of the movable baffle can effectively excite resonance in ARMs, enabling highly efficient and narrowband anomalous reflection.

Conclusion

In summary, we have proposed an acoustic resonance metagrating with a simple architecture consisting of air grooves and a mechanically translatable baffle. By translating the baffle, the higher-order guided mode in the widened groove transitions from evanescent to propagating. When the FP resonance condition is satisfied, this higher-order mode strongly interferes with the fundamental mode, exciting a Fano resonance that enables highly efficient anomalous reflection within a narrow frequency band. Theoretical and numerical analyses show that the anomalous reflection efficiency exceeds 99.9%. By examining the shape of the frequency spectrum, we further confirm the presence of Fano resonance. Moreover, through mechanical tuning of the movable baffle in the fabricated sample, we experimentally demonstrate efficient switching between anomalous and specular reflection. The measured efficiency can be further improved by reducing propagation losses, minimizing ambient noise, and optimizing the experimental setup. Our research not only provides a new solution for developing high-Q acoustic metagratings, but also opens new opportunities for the design of reconfigurable acoustic devices.

Data Availability

The data supporting the findings of this study are available from the corresponding authors upon reasonable request.

Acknowledgements

This work was supported by the National Key R&D Program of China (Grant Nos. 2022YFA1404400 and 2022YFA1404301), the

Startup Foundation for Introducing Talent of NUIST (Grant No. 1513142501019), the National Natural Science Foundation of China (Grant No. 12274313), and the Gusu Leading Talent Plan for Scientific and Technological Innovation and Entrepreneurship (Grant No. ZXL2024400).

References

[1] Hao Z, Chen H, Yin Y, Qiu C, Zhu S, and Chen H 2023 *Appl. Phys. Lett.* **123** 201702
[2] Zhou Y, Zhang T, Wang G, Guo Z, Zang X, Zhu Y, Ding F, and Zhuang S 2024 *Adv. Sci.* **11** 2406571
[3] Pan Z, Yang J, and Xu Y 2026 *Chin. Phys. Lett.* **43** 010401
[4] Fang X, Li S, Sun B, Yan D, Yang J, Luo J, Gao D, and Xu Y 2025 *Chin. Phys. Lett.* **42** 034301
[5] Quan J, Sun B, Wang F, Gao F, Fang X, Gao L, Hang Z, Chen H, Liu Y, Jiang J H, Fu Y, and Xu Y 2025 *Sci. Adv.* **11** eadw1701
[6] Kang M, Feng T, Wang H T, and Li J 2012 *Opt. Express* **20** 15882
[7] Alagappan G, García-Vidal F J, and Png C E 2024 *Phys. Rev. Lett.* **133** 226901
[8] Ataloglou V G and Eleftheriades G V 2025 *IEEE Trans. Antennas Propagat.* **73** 5346
[9] Ataloglou V G and Eleftheriades G V 2025 *IEEE Trans. Antennas Propagat.* **73** 4703
[10] Sun C, Gao J, Gao H, Ma X, and Huang X 2024 *Mater.* **17** 4730
[11] Li X, Wang Y, Fan J, He J, and Huang X 2022 *Appl. Sci.* **12** 7696
[12] Kim Y and Kim I 2025 *Light Sci. Appl.* **14** 204
[13] Shang X, Huang H, Zhou Y, Gong J, Liu Y, and Li W 2025 *Photonics* **12** 61
[14] Lin B, Huang W, Guo J, Huang B, Wang Y, Zhu R, and Wang Z 2023 *Opt. Commun.* **545** 129704
[15] Assouar B, Liang B, Wu Y, Li Y, Cheng J C, and Jing Y 2018 *Nat. Rev. Mater.* **3** 460
[16] Hao Z, Chen H, Yin Y, Zhu S, Xu Y, Qiu C W, and Chen H 2024 *Sci. China Phys. Mech. Astron.* **67** 264311
[17] Wang W, Hu C, Ni J, Ding Y, Weng J, Liang B, Qiu C, and Cheng J 2022 *Adv. Sci.* **9** 2203482
[18] Hao Z, Li S, Xu Y, Zhu S, and Chen H 2024 *New J. Phys.* **26** 093006
[19] Hao Z, Chen H, Yin Y, Qiu C W, Zhu S, and Chen H 2024 *Front. Phys.* **19** 42202
[20] Yu N and Capasso F 2014 *Nat. Mater.* **13** 139
[21] Dong H W, Shen C, Liu Z, Zhao S D, Ren Z, Liu C X, He X, Cummer S A, Wang Y S, Fang D, and Cheng L 2024 *Mater. Today* **80** 824
[22] Xu Y, Fu Y, and Chen H 2016 *Nat. Rev. Mater.* **1** 16067
[23] Meinzer N, Barnes W L, and Hooper I R 2014 *Nat. Photon.* **8** 889
[24] Hao Z, Guo X, Zhou Y, Yin Y, Xu Y, Chen H, and Qiu Z 2025 *J Appl. Phys.* **138** 133101
[25] Shi J, Li S, Liu Y, Liu Z, Wang X, Chen J, Liu X, and Liu G 2026 *Opt. Lett.* **51** 301
[26] Goldberg B, Zhang S, and Lawrence M 2025 *Adv. Opt. Mater.* **13** e00731
[27] Hail C U, Foley M, Sokhoyan R, Michaeli L, and Atwater H A 2023 *Nat. Commun.* **14** 8476
[28] Hao Z, Zhu S, Qiu C W, Xu Y, and Chen H 2024 *Chin. Opt. Lett.* **22** 033601
[29] Chen L, Yu Y, and Zhang X 2024 *Nano Lett.* **24** 12634
[30] Yao J, Lin R, Che X, Fan Y, Liang Y, Zhang J, Chen M K, and Tsai D P 2023 *ACS Photonics* **10** 4273
[31] Zaidi A, Rubin N A, Meretska M L, Li L W, Dorrah A H, Park J S, and Capasso F 2024 *Nat. Photon.* **18** 704
[32] Cao Y, Yu B, Fu Y, Gao L, and Xu Y 2020 *Chin. Phys. Lett.* **37** 097801
[33] Fu Y, Shen C, Cao Y, Gao L, Chen H, Chan C T, Cummer S A, and Xu Y 2019 *Nat. Commun.* **10** 2326
[34] Baspinar A B, Pearson P, and Faraon A 2026 *Adv. Optical Mater.* **14** e71282
[35] Yang C, Shen Z, Han D, Hou Y, Ji X, Zhang L, Yan R, and Chen X 2025 *Opt. Laser Technol.* **182** 112139
[36] Chen Y, Quan J, Gao Y, Sun B, Gao F, Fu Y, and Xu Y 2025 *Appl. Phys. Lett.* **126** 201704
[37] Zhang X, Li L, Li K, Liu T, Zhang J, and Hu N 2023 *Appl. Acoust.* **202** 109170
[38] Chen Z, Guan S, Xie Q, Li Z, Gao Z, and Negahban M 2023 *Front. Phys.* **10** 1098261
[39] Stirling C J, Nedeljkovic M, Mitchell C, Rowe D J, and Mashanovich G Z 2024 *Photonics Nanostruct.* **58** 101223
[40] Li X, Dong D, Liu J, Liu Y, and Fu Y 2022 *Appl. Phys. Lett.* **120** 151701
[41] Miroshnichenko A E, Flach S, and Kivshar Y S 2010 *Rev. Mod. Phys.* **82** 2257
[42] Xu Y, Fu Y, and Chen H 2015 *Sci. Rep.* **5** 12219
[43] Xie Y, Wang W, Chen H, Konneker A, Popa B I, and Cummer S A 2014 *Nat. Commun.* **5** 5553
[44] Zhou S, Dong S, He T, Zhu J, Wang Z, and Cheng X 2024 *Micromachines* **15** 538
[45] Bikbaev R G, Maksimov D N, Chen K P, and Timofeev I V 2022 *Mater.* **15** 6014
[46] Limonov M F, Rybin M V, Poddubny A N, and Kivshar Y S 2017 *Nat. Photon* **11** 543
[47] Gao Y, Quan J, Sun B, Xu L, Fu Y, Chen H, and Xu Y 2024 *Appl. Phys. Lett.* **124** 191701
[48] Li Y, Shen C, Xie Y, Li J, Wang W, Cummer S A, and Jing Y 2017 *Phys. Rev. Lett.* **119** 035501